



Strain controlled fatigue behaviour of a wire + arc additive manufactured Ti-6Al-4V

Abdul Khadar Syed^{a,*}, Rob Plaskitt^b, Michelle Hill^b, Zsolt Pinter^c, Jialuo Ding^d, Robert Zboray^e, Stewart Williams^d, Xiang Zhang^a

^a Faculty of Engineering, Environment and Computing, Coventry University, Coventry CV1 5FB, UK

^b Hottinger Bruel & Kjaer UK Ltd, UK

^c WAAM3D, UK

^d Welding Engineering and Laser Processing Centre, Cranfield University, Cranfield MK43 0AL, UK

^e Swiss Federal Laboratories for Materials Science and Technology (Empa), 8600 Dübendorf, Switzerland

ARTICLE INFO

Keywords:

Cyclic deformation

Low cycle fatigue

Strain controlled fatigue test

Titanium alloys

WAAM

ABSTRACT

This paper presents the cyclic deformation behaviour and fatigue properties of a wire + arc additive manufactured Ti-6Al-4V alloy in the as built condition under strain-controlled test condition. Higher local energy input used to build the material has resulted in a coarser primary columnar β grain structure along with a coarser α microstructure compared to Ti-6Al-4V alloys produced by other additive manufacture processes. Test specimens were manufactured in horizontal and vertical orientations with respect to the deposited layers. Isotropic fatigue property was observed at lower applied strain values. When the strain amplitude was above 0.6%, the vertical samples, where the loading axis was parallel with the primary columnar β grains, showed marginally higher fatigue life owing to the material being more ductile in this direction. Moreover, higher cyclic softening rate by a factor of two was measured in the vertical samples. No porosity defects were found in the material. Cracks were initiated from either the α laths or α/β interface due to cyclic slip localisation.

1. Introduction

One of the key requirements for additive manufactured (AM) materials is their performance under cyclic loading as it is paramount for safety-critical and load-bearing parts to satisfy the durability and damage tolerant design principles. If using powder feedstock in an AM process, the fatigue properties of Ti-6Al-4V (Ti64) are found to be lower than that of their wrought counterpart [1–8]. This is due to the presence of process inherent macroscopic defects that can act as stress raisers leading to fatigue crack initiation and premature failure. Post deposition heat treatments such as hot isostatic pressing (HIPing) showed promising results in improving fatigue strengths in most powder-based AM processes as it can effectively reduce the size and population of defects. Certain load bearing structures experience large plastic strains under a low number of load cycles (fatigue life $< 10^4$ cycles) before failure occurs. Under such conditions, Ti64 manifests cyclic softening behaviour where the applied stress amplitude gradually decreases until it stabilises. Sterling et al. [6] studied the fatigue behaviour of Ti64 built by laser blown powder AM process in the as built, stress relieved, and β annealed

condition. Samples in three conditions showed higher cyclic yield strength than those of wrought specimens due to the presence of α' martensite in the as built and finer α laths in the stress relieved and β annealed condition [6]. The fatigue lives of the laser blown powder specimens are shorter than the wrought due to premature failure from process inherent defects. The effect of microstructural anisotropy and the cyclic elastoplastic behaviour of L-PBF Ti64 when subjected to fully reverse loading (stress ratio $R = -1$) was studied in [9]. An asymmetric softening characterised by a vertical (i.e., stress) shift in the hysteresis loop under symmetric strain loading was observed. Agius et al. [9] claimed that the anisotropic plasticity was attributed to the considerable thermal residual stresses induced by the fast-cooling rate of 10^5 K/s, which in turn led to asymmetric cyclic yield.

Ren et al. [10] studied the strain-controlled fatigue properties of Ti64 processed by laser blown powder AM process in heat treated condition. By comparison with wrought Ti64, the fatigue performance of laser blown powder Ti64 was found to be lower at low strain amplitudes ($< 1.1\%$), while being similar at higher strain amplitudes. The presence of surface defects as small as $60 \mu\text{m}$ were claimed to be detrimental to

* Corresponding author.

E-mail address: abdul.syed@coventry.ac.uk (A.K. Syed).

<https://doi.org/10.1016/j.ijfatigue.2023.107579>

Received 11 October 2022; Received in revised form 23 December 2022; Accepted 14 February 2023

Available online 17 February 2023

0142-1123/© 2023 The Author(s). Published by Elsevier Ltd. This is an open access article under the CC BY license (<http://creativecommons.org/licenses/by/4.0/>).

the fatigue life [10]. In addition, cyclic softening is observed at various strain amplitudes where the degree of cyclic softening increased with the applied strain amplitudes [10]. Similar observations were made in [11] where the strain-controlled fatigue performance of L-PBF Ti64 was studied in the as built and heat treated (at 800 °C for 2 hours followed by furnace cooling) condition. Both the sample conditions showed cyclic softening behaviour. An increase in strain amplitude caused increased elastic modulus reduction occurred during the cyclic loading and promoted a greater cyclic softening [11]. In a recent study [12], Syed et al. systematically studied the cyclic plasticity and damage mechanisms in electron beam powder bed fusion (EB-PBF) Ti64 in the as built and HIPed condition. Samples were studied with the loading axis parallel to the primary columnar β grain. The cyclic stress–strain response of the as built samples was influenced by the α lath size. For the same applied strain amplitude, samples with smaller α lath showed a 2% higher stress amplitude and 38% lower plastic strain range compared to the samples with larger α lath. The authors have found that the cyclic softening response of samples in both conditions is driven by a monotonic reduction in the friction stress which represents the material isotropic hardening due to short-range interaction of dislocations with obstacles [13].

When considering higher deposition rate AM processes, Wire + Arc Additive Manufacturing (WAAM) has been extensively studied. In the as built condition, typical microstructure of WAAM Ti64 consists of multi-variant α colonies forming in the matrix (the so-called basketweave microstructure) and also single variant α colonies [14]. Depending on the build strategy, which influences the cooling rate, large microstructure heterogeneity is observed in WAAM built Ti64. Lower cooling rates resulted in larger α lath widths and its colony size [14]. The majority of the β grain boundaries had a continuous grain boundary α (α_{GB}) layer and outward growing single variant α colonies. However, some boundaries that may have had lower misorientation did not have a well-defined α_{GB} layer [14]. Columnar primary β grains resulted in 40% lower elongation in the samples loaded normal to α_{GB} facilitating a preferential path for local damage accumulation along the grain boundary [15]. The formation of such microstructure heterogeneity along the α_{GB} has been shown to influence material performance when subjected to cyclic loading. Recently, Syed et al. studied the role of anisotropy microstructure on high cycle fatigue performance of WAAM Ti64 built with different deposition strategies [15]. When α_{GB} was perpendicular to the fatigue loading, where the majority of the single variant large α colonies are under fatigue loading, this lowered the fatigue strength compared to samples loaded along the α_{GB} . Hence, fatigue property anisotropy was found.

Despite the progress made, the effect of plasticity on fatigue properties cannot be studied by stress-controlled fatigue tests. This is especially the case for the Ti64 alloy as it has little strain hardening capability after yield. Therefore, considering the practical applications, in which stress concentration is unavoidable for structural joints and cut-outs, it is critical to have a comprehensive understanding of the role of microstructure and sample orientation on strain-controlled fatigue performance to exploit the full potential of WAAM. Strain controlled fatigue testing will provide insights into the applied elastic–plastic strain energy that is driving fatigue failure. Accurate local strain measurement within the gauge length allows considerably greater precision to be achieved for the strain energy in the low-cycle plastic deformation region. The effect of plasticity is therefore reflected in the strain vs life property, which is useful for predictive models, which cannot be determined in load-controlled fatigue testing for the stress-life fatigue property. Strain controlled fatigue testing allows a more rigorous and reproducible definition of failure than in load-controlled testing. Furthermore, applied loads in strain-controlled fatigue tests are fully reversed, with applied strain ratio $R_e = -1$ i.e., zero initial mean stress, to provide the baseline fatigue data from which the mean stress effect can be calculated, as in the variable amplitude load spectra in real world loading conditions. Additionally, because strain-life fatigue curves are

based on the local strains, they are better suited to the predictive methods using the local stress or strain values, e.g., calculated by finite element analysis than using stress-life fatigue curves which are based on the nominal (applied) stresses. Therefore, this paper is focused on the strain-controlled fatigue behaviour, associated cyclic deformation and damage mechanisms of Ti64 deposited with oscillation build strategy developed for the WAAM process. The samples were tested in horizontal (α_{GB} perpendicular to the loading) and vertical (α_{GB} along the loading) orientations.

2. Materials and experimental methods

2.1. Materials manufacturing

Ti64 material was deposited by the WAAM process using a plasma arc as energy source and a 1.2 mm diameter Ti64 wire as a feedstock. Argon gas of 99.99% purity was used to create an inert atmosphere during the deposition. The process parameters were as follows: torch travel speed 5–6 mm/s, wire feed rate 2.5 m/min, arc current 200 A, plasma gas flow of 0.8 l/min and a shielding gas flow of 8 l/min. An oscillation building strategy (parallel square pattern) was used to deposit the materials where the plasma torch and the wire feeder were continuously oscillated across the wall thickness direction (TD) with 60–66% overlap between the adjacent melt tracks. During the deposition of subsequent layers, an alternating building direction between the layers was chosen to allow a continuous deposition without arc being turned off and on for depositing subsequent passes, thus, the total fabrication time is minimised. Two walls were deposited with dimensions in length (L) \times height (h) \times thickness (t) of 500 \times 150 \times 20 mm³.

2.2. Microstructure and texture analysis

Samples for microstructure and electron back scattered diffraction (EBSD) analysis were cut from the TD-ND plane and prepared with standard metallographic procedures with final polishing using colloidal silica with a 0.02 μ m particle size. For microstructure analysis samples were etched with Kroll's reagent and imaged with Zeiss LSM 780 optical microscope and a Zeiss Gemini Sigma 500VP scanning electron microscope (SEM). For α lath width measurements, cross-section samples were extracted from the WD-ND planes at the midpoint of each wall. Secondary electron SEM images taken from these samples were used to measure the average α lath linear intercept width in each build, according to ASTM E1382 standard [16], using the procedure described in detail in [17]. The length of the intercepts across each line was determined using the Image-J software. EBSD orientation maps along ND-TD plane were obtained using an FEI Sirion SEM, equipped with an Oxford Instruments' Nordlys Nano EBSD detector and AZtec acquisition software, using an accelerating voltage of 20 kV a beam current of 1.7nA across an area of 400 μ m \times 400 μ m. A step size of 10 μ m for low resolution maps and 0.3 μ m for high resolution maps were used. β -phase orientation maps were reconstructed from the indexed α -phase data, using software developed by Davies and Wynne [18,19] that exploits the BOR between the α and β phases. A maximum 3° divergence from the BOR was accepted, and a 2° misorientation of each α variant was allowed. The EBSD maps were produced in Oxford Instruments' Channel 5 software. All EBSD maps are presented in IPF colouring, with respect to the build-height direction (ND).

2.3. X-ray micro computed tomography analysis

Prior to testing, randomly selected samples were examined using micro X-ray computed tomography (micro-XCT) on RX Solutions Easy-Tom XL Ultra 230–160 scanner. The X-ray tube was operated at 180 kV acceleration voltage and a tube current of 70 μ A. The X-ray beam has been pre-filtered placing a 0.7 mm thick Cu plate on the tube to decrease

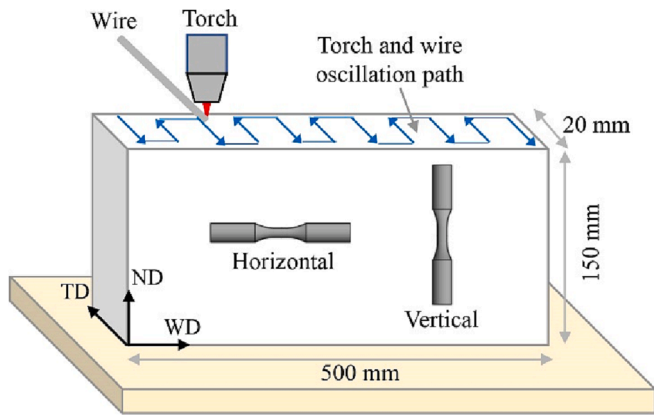


Fig. 1. Schematic of a WAAM Ti64 wall showing the torch and wire oscillation path and test sample orientations used for tensile and strain-controlled fatigue tests. WD - the heat source travel direction, TD - wall transverse or thickness direction, ND - build height direction normal to the deposited layers.

beam hardening artefacts. The detector used was a Varian 2520 flat panel with 1920×1536 pixels of $127 \mu\text{m}$ pitch with columnar CsI as scintillating material. First a standard, circular-trajectory cone-beam scan was performed concentrating on the center part of the sample capturing a height of 6.5 mm and a volume diameter of 5.7 mm. After that a helix scan was performed to capture a longer axial section of the sample object with 3 full turns (360°) of rotation around the object. The number of projections per turn was 1152 (just as for the circular scan). The total scanned volume was 15.5 mm tall with a diameter of 5.7 mm. For both scans, for each projection 10 image frames have been averaged, taken at a frame rate of 4 fps resulting in a total scan time of roughly 3 h helix and roughly 1 h for the circular scan. The geometric magnification, based on the ratio of source-to-detector and source-to-sample distance for both scans was around 33. For the 3D reconstruction (filtered back projection) the FDK algorithm [20] was used in the native software of the scanner XAct of RX solutions. The isotropic voxel size of the

reconstructed volume was $3.88 \mu\text{m}$ for the helix and slightly lower, $3.7 \mu\text{m}$, for the standard circular scan. The 3D image processing and rendering has been performed by the commercial software VG Studio Max 3.5 from Volume Graphics.

2.4. Mechanical testing

Tensile and strain-controlled fatigue test samples were manufactured in either “horizontal” or “vertical” orientation as defined in Fig. 1. In the horizontal sample, the loading axis is parallel to the deposited layers (across columnar β grains and α_{GB}), whereas in the vertical sample the loading axis is perpendicular to the deposited layers (along columnar β grains and α_{GB}). Tensile test samples were designed according to the ASTM E8 standard [21] with a gauge diameter and gauge length of 5.75 mm and 31 mm, respectively. The tests were performed according to the ASTM E8 standard [21] with an applied displacement rate of 1 mm/min, and the strain was measured with a 25 mm gauge length clip-on extensometer. Strain controlled fatigue test samples were designed and tested according to the ASTM E606 standard [22]. A gauge diameter 5 mm and gauge length 10 mm were used. Applied strain was measured and controlled by a 10 mm gauge length clip-on extensometer. Prior to testing, the gauge section of each fatigue specimen was polished along the longitudinal axis to remove any surface imperfections from machining that could act as undesirable fatigue initiation points. Specimens were polished using a Morrison test specimen polishing machine using various grades of grit paper and finishing with 1200 grit paper to achieve a minimum surface roughness specification $R_a = 0.2 \mu\text{m}$ in accordance with the BS7270 and ASTM E606 standards. Strain controlled fatigue tests were carried out at room temperature in fully reversed mode (strain ratio $R_e = -1$) at total strain amplitudes ($\Delta\epsilon/2$) ranging between 0.4% and 1.2%. The test frequency for each fatigue test was varied according to the strain level of the test, and the material response to maintain the sinusoidal waveform, from 0.25 Hz at the highest strain range to 5 Hz at the lowest. Fatigue life was defined at a number of cycles when the stress response dropped by 20% from the stabilised stress-strain curve.

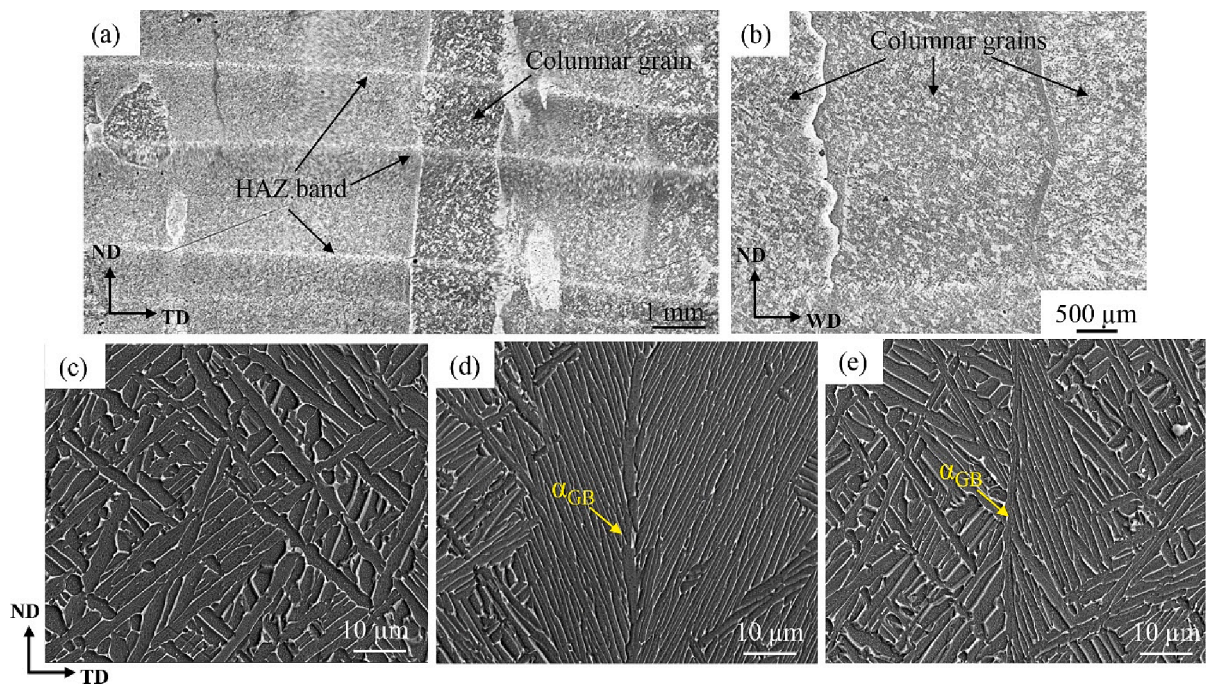


Fig. 2. (a), (b) optical micrographs showing epitaxially grown columnar grains and HAZ bands in the wall's ND-TD and ND-WD planes. SEM images showing (c) typical transformation bulk microstructure, (d) transformation microstructure along primary β grain boundaries with continuous boundary α colonies and (e) discontinuous α colonies along the primary β grain boundaries.

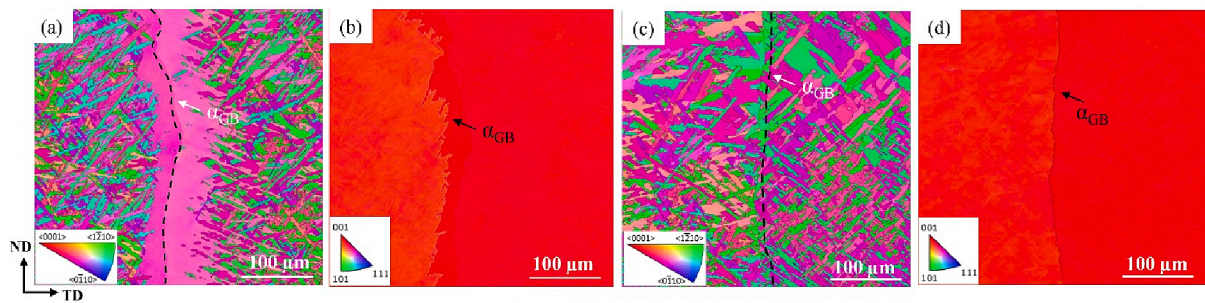


Fig. 3. EBSD maps along the ND-TD plane showing (a) and (c) α phase with and without continuous α colonies, (b) and (d) respective reconstructed β phase. All EBSD maps are presented in IPF colouring, with respect to the build-height direction (ND).

3. Results and discussion

3.1. Microstructure heterogeneity

It is well documented that the layer wise deposition in AM gives rise to macroscopic heterogeneity of the microstructure in the form of columnar primary β grains aligning in parallel to the build direction [9]. The WAAM layer deposition strategies [14] generally produce wider columnar primary β grains compared to other AM processes. Oscillation build strategy used to deposit the current materials produces much wider columnar primary β grains (width ranging between 0.43 and 3 mm) compared with other deposition strategies available in WAAM [14], Fig. 2a and 2b. In addition to the steep positive thermal gradient at the solidification front in a heated melt pool and low solute partitioning in Ti64 alloy, the local thermal condition influenced by the heat source travels along the WD direction and oscillates along the TD during the build resulting in wider primary β grains. These coarse-columnar primary β grains span a few millimetres in length and have grown through multiple layers along the build direction. The combination of large layer

increments and local thermal history in the high deposition rate AM processes such as WAAM leads to lower solidification velocities resulted in heat affected zones (HAZ) bands [23], which are regularly spaced along the build direction as shown in Fig. 2a. The microstructure heterogeneity caused by the HAZ bands in different AM processes is of particular interest [23–26]. The majority of these studies are based on qualitative observation. Nevertheless, Ho et al. [23] utilised a multi-scale approach to quantify important characteristics of HAZ banding regions in WAAM Ti64 deposited with single and multi-parallel pass build strategies. According to the study in [23], HAZ bands in WAAM are the consequence of temperatures reaching just below the β transus temperature in previously deposited layer during the subsequent layer deposition. Such continuous thermal cycles lead to a strong microstructure divergence in the HAZ bands region. Within the HAZ bands, coarsening of the lamellar transformation structure and the formation of a thin layer with a finer α lamellar single variant colony microstructure just below the β transus (~ 990 °C) is observed. Further detailed discussion on the mechanism and evolution of the diverse microstructure in and around the HAZ bands are discussed in detail in [23].

The complex cyclic thermal history associated with solidification of sequentially deposited layers led to a systematic variation in the transformed microstructure resulting in large microstructure heterogeneity which can be found in some of the examples presented in Fig. 2c-2e. Such microstructure heterogeneity in the as built condition is present in a majority of the AM processes. It is well documented that this microstructure heterogeneity is strongly affected by the cooling rate below the transus during the initial solidification [27], which is later influenced by the thermal exposure during the subsequent reheating at temperatures near to, but below the β transus [23]. The typical transformation microstructure within the bulk material consists of classical lamellar $\alpha + \beta$ microstructures, with both Widmanstätten multi-variant (basketweave) and single variant colony morphologies, Fig. 2c. The average α lath width was measured as 2.3 ± 0.2 μm . In comparison to other AM processes [28], a coarser α lath spacing was seen in this study. In the WAAM build, the repeated oscillation of torch and feeder across the WD-TD to achieve the desired wall width not only creates an asymmetry in the thermal field but also a greater build-up of heat resulted in a slower cooling rate. Thus, a coarser α lath spacing is seen in WAAM especially when using an oscillation build strategy. Transformation microstructures seen across a β grain boundary are also shown in Fig. 2d and 2e. Owing to the Burgers orientation relationship (BOR) and the tendency for grain boundary (GB) nucleation, the solidification structure led to a strong local microstructure variation along the grain boundary α (α_{GB}). 83% of the primary β GBs studied had a continuous α_{GB} layer with continuous α_{GB} colony which has an angle of $\sim 90^\circ$ between neighbouring α lamella growth directions, refer Fig. 2d. A primary β GB without continuous α_{GB} from this same sample is shown Fig. 2e with outwardly growing multi-variant α colonies forming in the matrix (basketweave or Widmanstätten microstructure, Fig. 2e). In general, the single variant α colonies extended further into the grains that are a result of much slower cooling rate during the $\beta \rightarrow \beta + \alpha$ transformation with

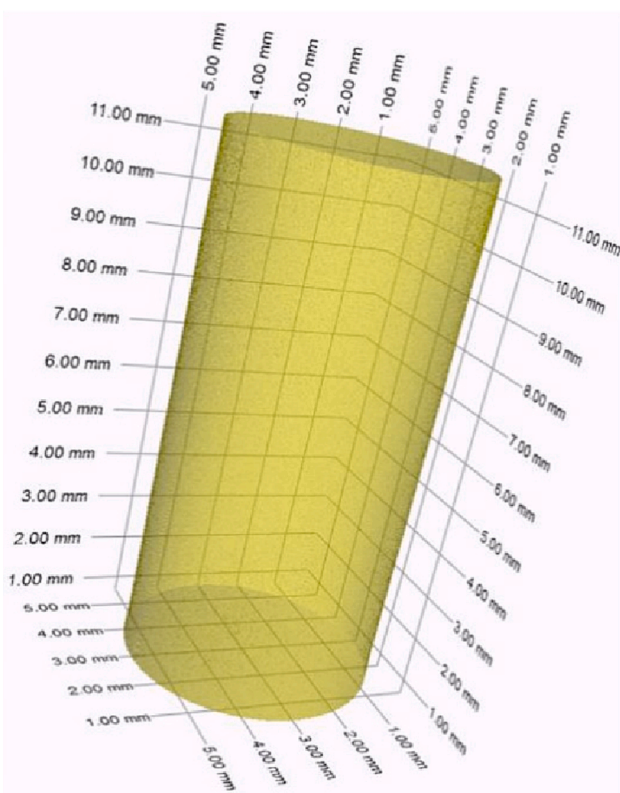


Fig. 4. Micro-XCT results in the gauge section of a specimen illustrating 3D rendering of the sample with 60% transparency showing no porosity.

Table 1
Tensile properties of Ti-6Al-4V obtained from the engineering stress–strain data.

Material property	WAAM		Wrought (AMS 4928)	Cast (AMS 4992)	ASTM F2924
	Horizontal	Vertical			
Yield strength ($YS_{0.2}$), MPa	842 ± 14	800 ± 23	861	765	825
Ultimate tensile strength (UTS), MPa	951 ± 12	898 ± 24	930	861	895
Elongation (%)	11 ± 2	17 ± 5	25	5	10

WAAM process. These single variant α colonies across the α_{GB} depicts a strong crystallographic texture [29]. β grains in WAAM share a common neighbouring grains $[110]_{\beta}$ which exclusively led to the nucleation of continuous α_{GB} colonies either side of the primary β GB [29]. Some prior β grain boundaries are also decorated with a mixture of multivariant and single variant α colonies on either side it is showing the typical solidification in AM [26,30].

Fig. 3a and 3c shows EBSD maps along the primary β grain with and without continuous grain boundary α colonies respectively and corresponding reconstructed β phases are present in Fig. 3b and 3d. respectively. The continuous α_{GB} colony is more pronounced and thicker compared to the primary β grain boundary with multi-variant α colonies. The continuous α_{GB} growing off the primary β grain boundaries in Fig. 3a can be seen to have similar orientations either side of the grain boundary. In Ti64, single variant α_{GB} colonies will develop discontinuously with larger α lamellae nucleating first at lower undercooling [31]. These

single variant orientation along segments of β grain boundaries grow out rapidly and form skeletal variant templates from which the subsequent colonies will develop as the temperature falls and transformation progresses [31]. On the other hand, grain boundaries without continuous α_{GB} colonies can be seen to have nucleated numerous α orientations, none of which cross the primary β grain boundaries into the neighbouring grains. The α lamellae in the prior β grain interiors largely have a typical basketweave morphology with a high aspect ratio. It is well known that the α nucleation is affected by BOR and the local β grain boundary plane and its misorientation [32]. Continuous α layers have been also observed decorating β grain boundaries in conventionally built Ti64 [33,34].

The micro-XCT analysis results are presented in Fig. 4. The sample has been found very homogeneous showing no sign of defects or porosity down to the resolution limit. This was $\sim 7.4 \mu\text{m}$ taken as the Nyquist limit for the isotropic voxel sampling. This homogeneity is illustrated in the 3D rendering of the helix scan in Fig. 4.

3.2. Tensile properties

Tensile properties obtained from the engineering stress–strain data are presented in Table 1 along with conventionally manufactured Ti64, i.e., AMS 4928 wrought bar [35], annealed (12.7 mm thickness), casting [35], HIPed and annealed (< 12.7 mm thickness) and minimum tensile properties recommended for AM Ti64 by ASTM F2924 [36]. WAAM Ti64 tensile strengths are comparable with its wrought counterpart, higher than the cast material and the minimum tensile property requirements specified in ASTM F2924 for AM built Ti64 [36]. In terms of the elongation property, WAAM Ti64 horizontal and vertical samples

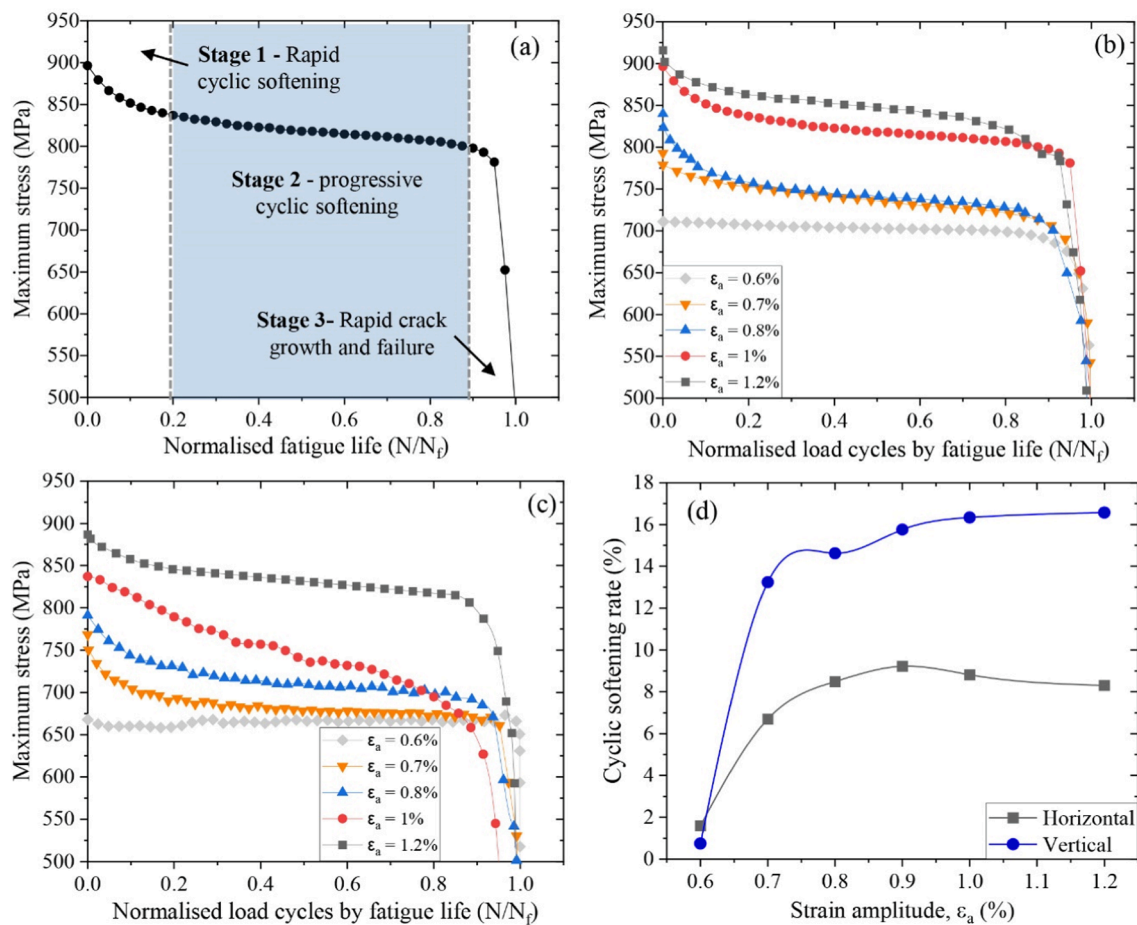


Fig. 5. (a) Maximum stress vs normalised load cycles illustrating three distinct stages of the cyclic stress response under strain-controlled test. Cyclic maximum stress vs normalised load cycles for (b) horizontal and (c) vertical samples, (d) cyclic softening rate under different strain amplitudes.

were 2 and 3 times higher than that of cast material, but 2.4 and 1.7 times lower than that of the wrought material. In Ti64, plastic deformation is predominantly controlled by the high volume fraction (~90–95%) of the α phase [37]. It is generally accepted that the Widmanstätten microstructure present in AM Ti64 exhibits lower ductility than the equiaxed or bimodal microstructures present in wrought condition due to the presence of typical larger α colony and larger α lath widths.

Horizontal samples showed higher yield and tensile strengths compared to the vertical samples, whereas higher elongation was found in the vertical samples. The anisotropy in ductility is generally observed in AM built Ti64 [28,38–40] which is linked to the epitaxially grown primary β grains. It has been shown that α variant greatly influence the mechanical properties in AM Ti64 [41]. Material with single variant α colonies showed a stronger crystallographic texture which increased the effective slip length and allowed the dislocations to move freely within the colonies during the tensile deformation. This has resulted in early voids formation and lower ductility [41]. The lower ductility in the horizontal samples of current study can be also linked to the presence of large α colonies at the primary β grain boundary which is normal to the tensile axis. During the tensile deformation, the dislocation motions were precluded by the size and different orientation α phase. The local pile up of dislocations during the deformation will lead to stress concentration along the α/β interface thereby voids and fracture formation. When the primary β grain boundary is normal to the tensile axis, the dislocation can slip freely inside the large α colonies present at the primary β grain boundary, due to the parallel α plates sharing the same orientation and leads to early void formation.

Recently Tseng et al. [42] studied the influence of columnar grains on anisotropic deformation mechanisms in L-PBF Ti64 using samples with the tensile axis parallel and perpendicular to the columnar primary β grains. Anisotropic tensile properties were caused by strong columnar texture associated with the columnar primary β grains. When the samples are loaded normal to the columnar primary β grains ($10\bar{1}1$) crystallographic planes were in-plane with the tensile axis which is dominant plane for plastic deformation. The majority of the plastic strain were accumulated in ($10\bar{1}1$) and led to the development of $\{10\bar{1}1\}$ growth faults. As a result, higher YS, UTS and a lower ductility is found in horizontal samples [42]. In contrast, tensile loading normal to the primary β columnar grains and α_{GB} in horizontal samples facilitate a preferential path for strain accumulation, early void formation thereby crack nucleation leading to early fracture and lower ductility [43]. Conversely, the higher elongation in vertical samples is the result of a combined effect of the bulk microstructure (α lath size) and α_{GB} parallel to the loading axis which has contributed to the plastic deformation, thereby increased ductility [43]. Similar results were observed in L-PBF Ti64 when the tensile axis parallel to columnar primary β grains where (0002) plane was observed as a stacking structure which was aligned at an angle of $< 30^\circ$ to the tensile direction. In addition, Tseng et al. [42] also observed a twist-like distortion of the crystallites between distinct layers or within one build layer. Such a stacking structure along with twist like distortion resulted in a strong correlation between the (0002) and ($10\bar{1}1$) planes and the major deformation was observed along the (0002) tensile direction and led to quicker rupture and lower tensile properties [44,45].

3.3. Cyclic deformation behaviour

Under cyclic loading material damage is progressive which develops as a consequence of dislocations rearrangement and persistent slip bands leading to localised plastic deformation. The cyclic response of materials depends on the test conditions, microstructure and its constituents that are influenced by their processing route. In the case of AM built materials, sample orientation also plays a major role on the cyclic deformation and damage mechanisms. Amongst these, the effect of sample

orientation and applied strain amplitudes are the two variables investigated in this study. The progression of cyclic stress versus normalised load cycles (N/N_f , where N is the cycle number and N_f is the number of cycles to failure) is presented in Fig. 5. The progression of cyclic stress amplitude (or maximum stress) versus number of cycle response during strain-controlled fatigue testing can be divided into three distinct stages, refer Fig. 5a. *Stage 1* represents a rapid cyclic softening where a steep decrease in applied stress amplitude (or maximum stress) is observed. The material will spend briefly 5–15% of the total fatigue lifetime in stage 1. In general, materials will reach a stable hysteresis loop after stage 1. *Stage 2* represents a progressive quasi-stable cyclic response that occupies the majority of the cyclic lifetime (75–80% of total fatigue life) where a noticeable and continuous cyclic softening (change in the stress amplitude or maximum stress) is observed. *Stage 3* is the final stage governed by rapid fatigue crack propagation leading to failure; this stage manifests itself by a rapid decrease in the stress amplitude.

Fig. 5b and 5c presents the progression of maximum stress versus number of cycle response for both the samples orientations. In general, cyclic softening is apparent in both of the sample orientations under different strain amplitudes, except when $\Delta\epsilon/2 \leq 0.6\%$ where elastic deformation is dominant. Three distinct stages are observed for both sample orientations when the applied strain amplitudes are $< 0.6\%$. The absence of stage 1 in samples tested at $\Delta\epsilon/2 \leq 0.6\%$ is apparent as the applied strain amplitudes are essentially elastic. When comparing both the sample orientations in stage 1, in all the cases, horizontal samples showed 2–4% higher peak stress compared to vertical samples. It is well documented that the mechanical properties and the rate of plastic deformation in titanium and its alloys depend on the size, morphology, and volume fraction of the α and β phases and their crystallographic orientation with respect to the loading axis [46–50]. The higher peak stress in the horizontal samples is associated with the columnar primary β grains that are aligned perpendicular to the loading axis and strong crystallographic texture along the α_{GB} . Primary β grains normal to the loading axis reduced the effective grain size in the loading direction, resulting in a higher strength due to the phenomenological Hall-Petch effect. In addition, strong crystallographic texture along the α_{GB} restricts the dislocation motions which will lead to higher strength values. Furthermore, the study reported in [51] also demonstrated that the interaction between grain shape and different textures (crystals and their slip systems), where each grain shape and slip plane have an effective grain size based on how the slip plane bisects the elongated grain, also contributes to anisotropic plastic deformation. Tseng et al. [42] studied the influence of columnar grains on deformation mechanisms in L-PBF Ti64 using in-situ synchrotron X-ray diffraction and complementary EBSD analysis. This study demonstrated that the samples loaded perpendicular to the columnar grains accumulated larger plastic strains in the measured crystallographic orientations, particularly the ($10\bar{1}1$) plane accumulated more pronounced elastic and plastic strains. According to [42], such distinctive directional deformation is correlated with the crystallographic texture where vertical samples have highly preferentially orientated $\alpha+\beta$ with respect to the loading axis, which leads to lower plastic strain accumulation. On the other hand, horizontal samples had randomly oriented crystallographic planes with respect to the loading axis which is leading larger plastic strain accumulation and higher stresses compared to the vertical samples. In stage 2, a plateau in the stress response was not reached in any sample, except in $\Delta\epsilon/2 \leq 0.6\%$ due to elastic stresses. As stage 3 is governed by crack initiation and rapid crack propagation, all the samples showed a rapid decrease in the maximum stresses at $N/N_f \approx 0.95$. The cyclic deformation and the damage mechanisms are related to the damage accumulation rate. Therefore, to illustrate the cyclic softening extent and the influence of sample orientation on it, a cyclic softening rate (CSR) under a given strain amplitude was determined using equation (1) [52].

$$CSR = (\Delta\sigma_{max} - \Delta\sigma_{half}) / \Delta\sigma_{max} \quad (1)$$

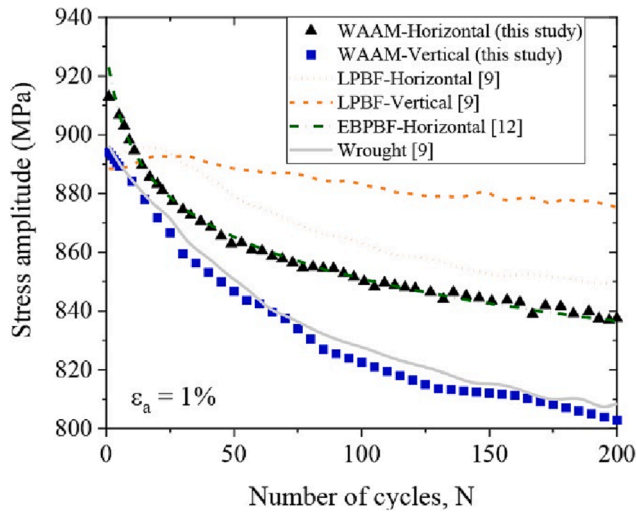


Fig. 6. Changes in the stress amplitude vs the load cycles for as built waam ti64 (this study) in comparison with the literature data for laser powder bed fusion (L-PBF) [9], electron beam powder bed fusion (EB-PBF) [12] and conventionally built wrought [9]. All data correspond to the applied strain amplitude 1%.

where $\Delta\sigma_{\max}$ is the maximum applied stress range during the test and $\Delta\sigma_{\text{half}}$ is the stress range at half stage of the fatigue lifetime.

Fig. 5d shows that the cyclic softening rate for both sample orientations is similar at lower strain amplitude (i.e. $\epsilon_a \leq 0.6\%$). Beyond this, it increased dramatically in both sample orientations, from $\sim 1.6\%$ to 6.7% for the horizontal and $\sim 0.75\%$ to 13.2% for the vertical samples at $\epsilon_a = 0.7\%$. Beyond this post, the cyclic softening rate stabilised manifesting a plateau response. In addition, Fig. 4d shows that the vertical samples showed higher cyclic softening rate compared to horizontal samples. In particular the vertical samples showed approximately-two times higher cyclic softening rate when $\epsilon_a \geq 0.7\%$. According to the above results, we can infer that the cyclic stress response and damage behaviour is influenced by the sample orientation in AM built Ti64 owing to the microstructure anisotropy.

Ti64 microstructures produced by various AM processes are significantly different from the conventionally built by wrought or cast processes. A comparison between different Ti64 built by various AM processes provides insights into the influence of AM process and microstructure on cycle stress response mechanisms. All the data presented in Fig. 6 was tested at the same applied strain amplitude of $\epsilon_a = 1\%$. Compared to L-PBF, WAAM samples in both orientations showed a marginal higher stress amplitude, particularly the horizontal samples showed 3% higher cyclic stress amplitude compared to L-PBF horizontal sample. In the as built condition, L-PBF Ti64 is known to have acicular α' martensite resulting in higher yield strength compared to other AM built Ti64. However, the presence of α' phase and residual stresses in the L-PBF is responsible for a lower cyclic amplitude stress. In addition, WAAM samples showed continuous cyclic softening from the 1st cycle with higher cyclic softening rate compared to L-PBF where an initial cyclic hardening before the activation of cyclic softening. The acicular α' phase has been shown to have a high dislocation density [9,53], stacking faults and twin structures, all of which will cause dislocation tangling at the α' grain boundaries leading to initial cyclic hardening in the first few cycles. As the fatigue cycles progress, the dislocation can move across the grain boundary and initiate cyclic softening. On the other hand, EB-PBF and wrought built Ti64 shows similar cyclic softening behaviour as WAAM samples as all these processes resulted in fully transformed $\alpha + \beta$ with Widmanstätten and colony morphologies. Moreover, the absence of dislocation tangling characteristics also leads to a continuous cyclic softening in both EB-PBF and wrought materials [9,12].

Materials subjected to cyclic loading experience progressive damage at both micro and macroscopic levels which will influence the material

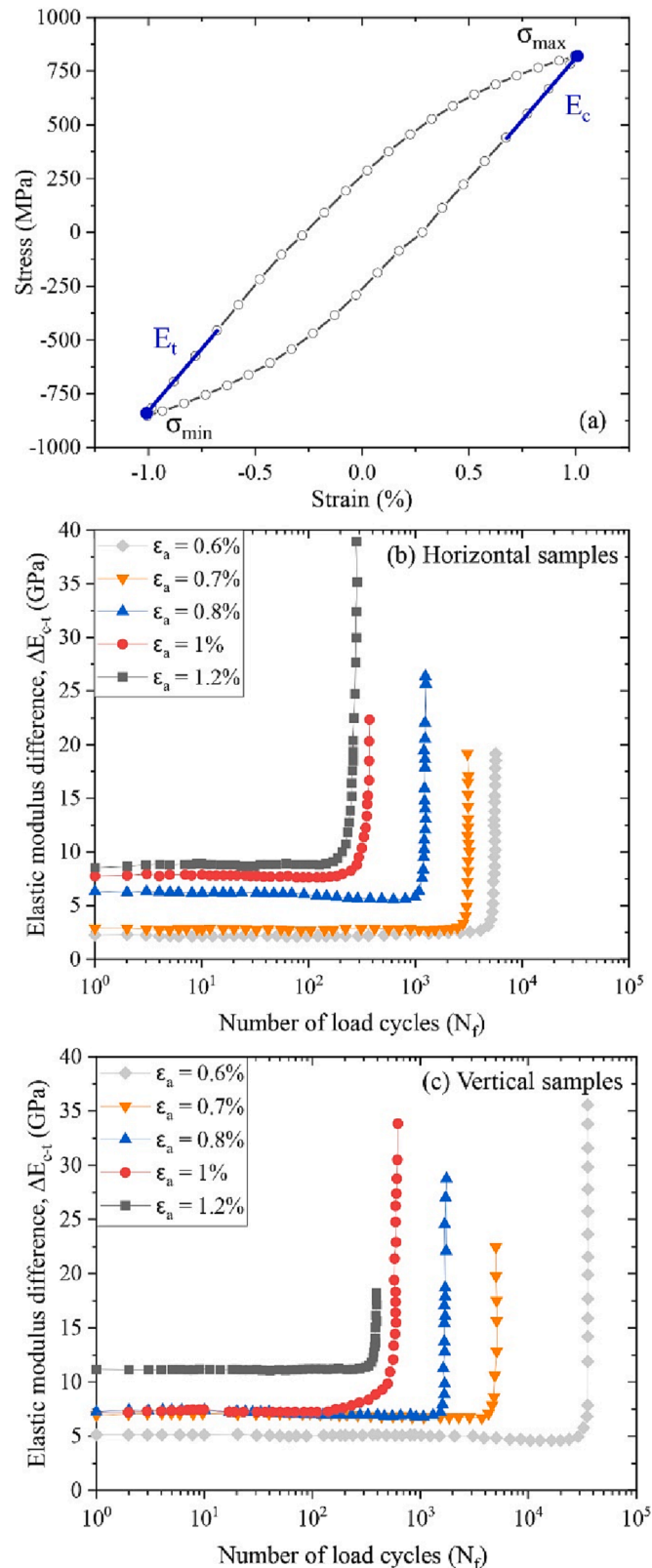


Fig. 7. (a) Schematic showing evaluation of elastic modulus of the tension-going loading excursions (E_t) and the compression-going loading excursions (E_c). (b) and (c) the evolution of apparent elastic modulus over the number of load cycles for horizontal and vertical samples respectively.

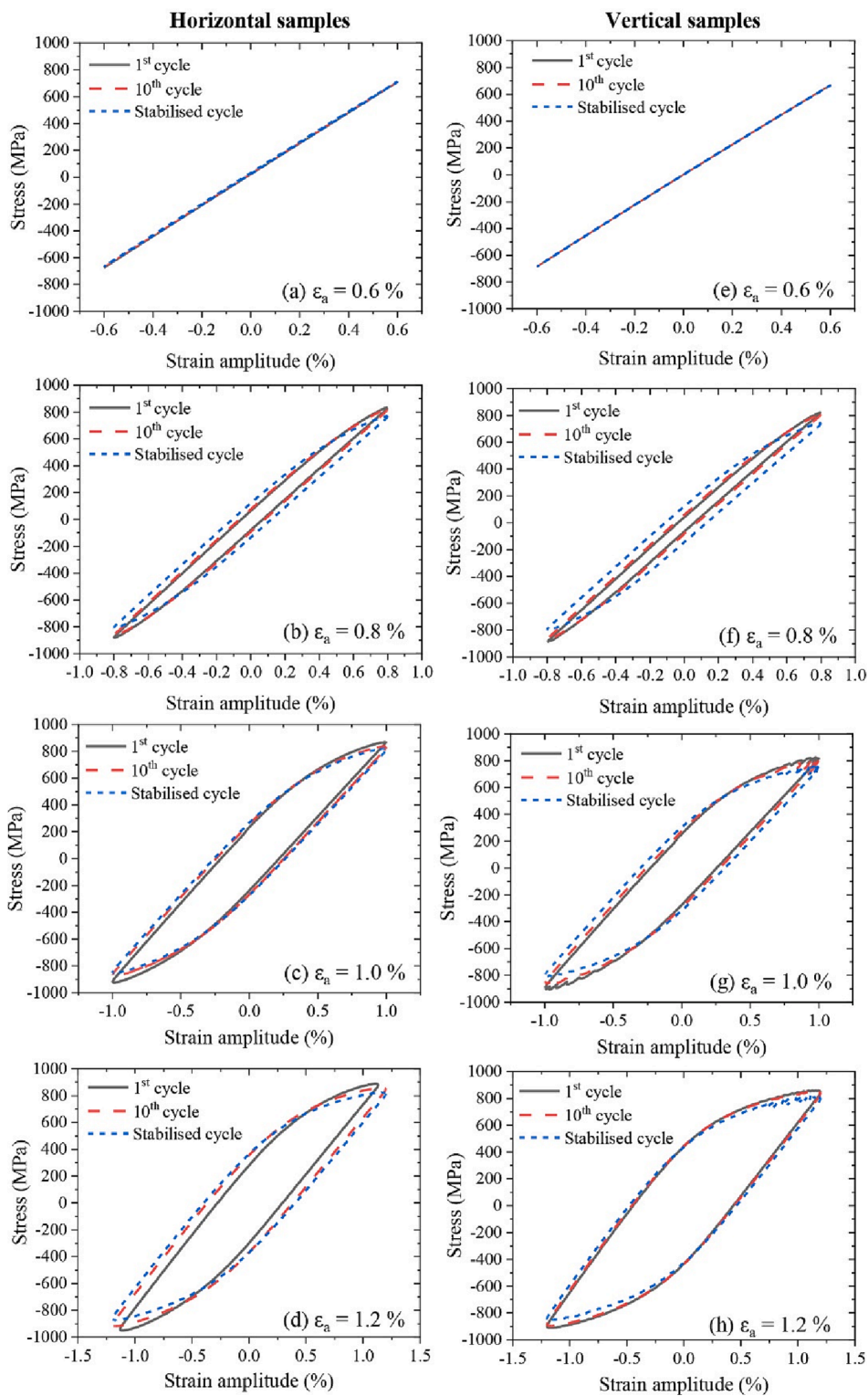


Fig. 8. Typical stress–strain hysteresis loops at different strain amplitudes and number of cycles for horizontal (a) – (d) and vertical samples (e) – (h).

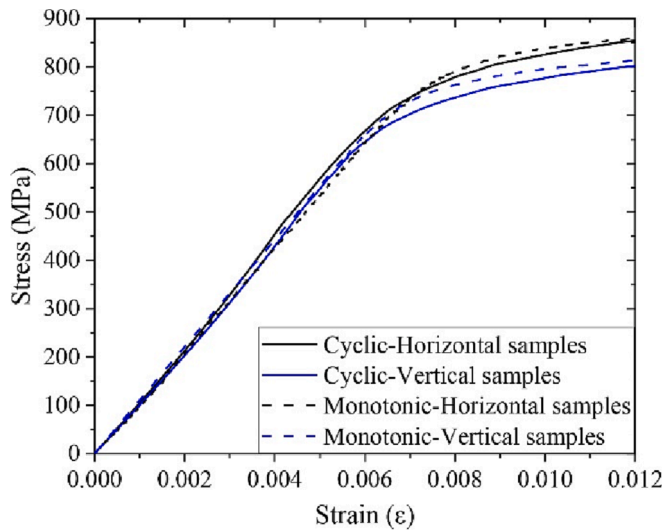


Fig. 9. A comparison of the cyclic and monotonic stress–strain curves.

behaviour and thereby performance. Under strain-controlled fatigue, progressive damage can cause reduction in the elastic modulus, especially at the loading excursions. This property degradation can be quantified by analysing the difference between the apparent elastic modulus in tension-going loading excursions (E_t) and the compression-going loading excursions (E_c) [54]. In general, the elastic modulus when the sample is being held in tension during the first part of the compression excursion (E_c) should be less than the modulus when the sample is under compression in the first part of the tension excursion (E_t) due to the difference in the microcracks or defects being open or closed. This difference between the apparent elastic moduli in compression and tension ($\Delta E_{c,t}$) becomes larger as the cracks propagate [54]. Therefore, the apparent tensile and compression elasticity modulus was measured as the slopes of the linear part of the respective excursions in the stress–strain hysteresis loops. A schematic of E_c and E_t evaluation is shown in Fig. 7a, and the evolution of the apparent elastic modulus difference over the number of load cycles is presented for horizontal and vertical samples in Fig. 7a and 7b respectively. It shows that the difference in the elastic modulus increased with strain amplitude which promotes cyclic softening. In both sample orientations, the elastic modulus difference is small ranging 2.5–11 GPa until load cycles reached 0.9–0.95 N_f . Beyond this point, a rapid increase in the modulus difference is observed. It has been reported that the reduction of macroscopic tensile load excursion is likely linked to the decrease in effective cross-sectional area as a result of the internal macroscopic crack formation and or propagation which are usually the consequence of persistent slip band formation during cyclic loading [9,11].

In general, materials subjected cyclic loading beyond the elastic regime exhibit either cyclic softening where cyclic stress decreases with cycle numbers or cyclic hardening where cyclic stress increases with cycle numbers. The cyclic hysteresis loops corresponding to the 1st, 10th and stabilised conditions for samples tested at different strain amplitudes are presented in Fig. 8. It can be observed that the hysteresis loops enlarged with the strain amplitudes. Two observations can be made. Firstly, with increasing number of cycles, the peak stress decreased at a given strain amplitude demonstrating the cyclic softening behaviour. Material behaviour under cyclic loading is influenced by the initial state of the material condition.

According to [10], the material belongs to soft state if the ratio between UTS and YS ≥ 1.4 that leads to the cyclic hardening phenomenon, whereas, if the ratio (UTS/YS) ≤ 1.2 , the materials belong to hard state

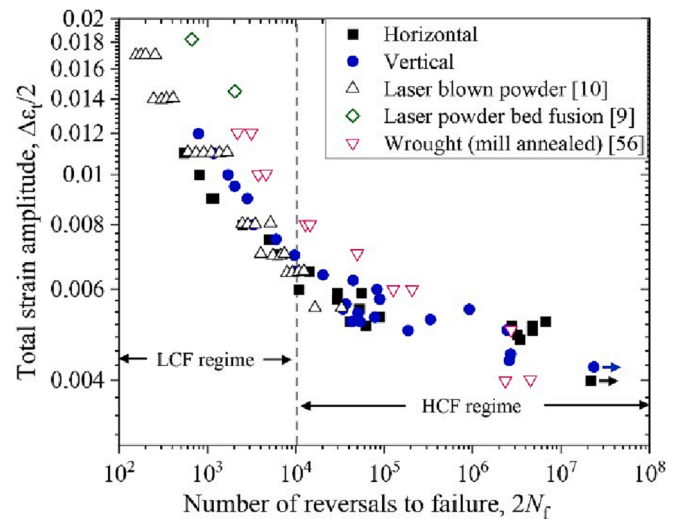


Fig. 10. Strain vs life relation measured by WAAM Ti64 samples. Literature data from other AM and conventional wrought processes are also presented for comparison.

and experience softening under cyclic loading. In the current study, both of the sample orientations exhibit UTS/YS ≈ 1.12 . Hence, cyclic softening is observed. Previous studies on wrought [9] and AM Ti64 also demonstrated cyclic softening behaviour [9,12,55]. Secondly, for the same applied strain amplitude, the vertical samples exhibit larger hysteresis loop areas than the horizontal indicating higher plasticity for the vertical samples which is also confirmed by the monotonic tensile properties presented in Table 1.

By connecting the tips of stabilised cyclic hysteresis loops corresponding to various applied strain levels, the cyclic stress–strain curve can be determined which is shown in Fig. 9 with a comparison with the monotonic stress–strain curves determined from tensile test. Fig. 9 confirms that materials in both sample orientations exhibited cyclic softening behaviour. At a given strain value beyond the yield point, the vertical samples showed lower stress indicating higher ductility in this material orientation.

3.4. Fatigue properties

The strain vs fatigue life properties are presented in Fig. 10. For comparison purpose, fatigue data of an equivalent conventional Ti64 material are also shown, taken from Ti64 extra low interstitials, mill annealed wrought hot rolled bar [56], together with a LPBF (as built condition) [9] and laser blown powder (as built condition) [10]. WAAM Ti64 showed lower fatigue properties than the mill annealed. When total strain amplitude ($\Delta\epsilon_t/2$) is > 0.006 , WAAM horizontal and vertical samples showed an average of 5.7 and 2.2 times lower fatigue life compared to wrought mill annealed material. Wrought Ti64 has higher ductility and lower yield strength owing to its equiaxed microstructure. On the other hand, WAAM Ti64 consists of Widmanstätten and single variant colony microstructure leading to higher strength and lower ductility. Plastic deformation in titanium alloys is accommodated by a complex mixture of crystallographic slip and deformation twinning [44,57]. Under strain controlled cyclic loading, fatigue life is dominated by crack growth. As a result, when the $\Delta\epsilon_t/2$ is > 0.006 , where plasticity dominates the fatigue life through crack closure, WAAM samples showed lower fatigue life. Nevertheless, when the $\Delta\epsilon_t/2 < 0.006$, where the applied stresses are within the elastic regime, i.e., no influence of plasticity, WAAM showed similar fatigue properties as wrought Ti64.

In general, there are two approaches to evaluate the strain-life data.

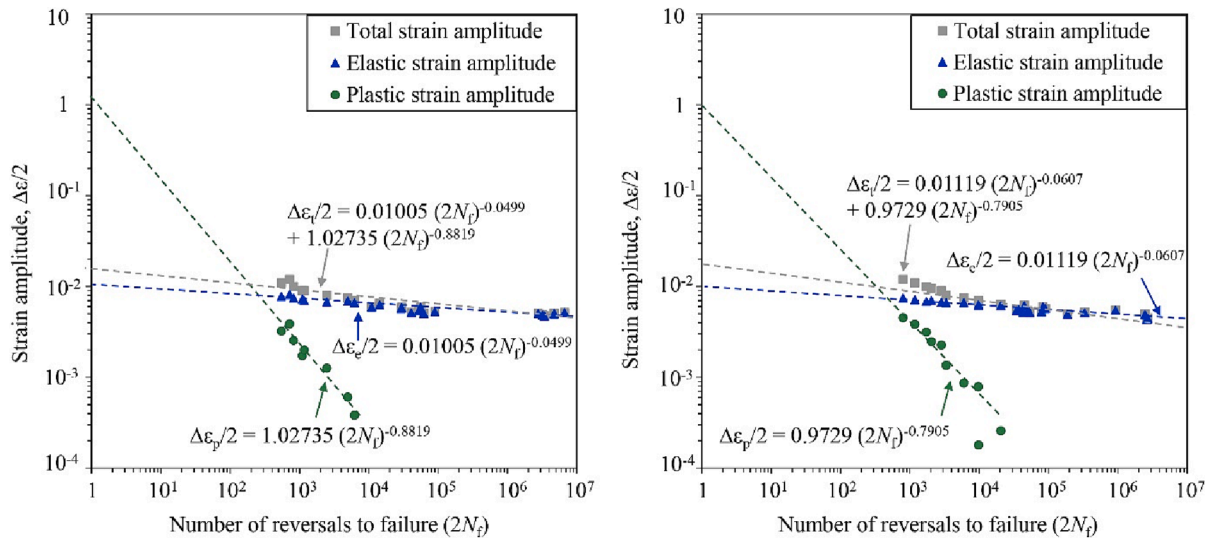


Fig. 11. Fitting lines of the measured data by the total strain, elastic strain (Basquin equation), and plastic strain (Coffin-Manson equation) for (a) horizontal and (b) vertical samples.

Table 2
Fitting parameters for the Basquin and Coffin-Manson equations.

Fit parameter	Horizontal sample	Vertical sample
E (GPa)	113.8	113.5
σ'_f (MPa)	1143.7	1270.1
b	-0.0499	-0.0607
e'_f	1.0273	0.9729
c	-0.8819	-0.7905

Coffin and Manson [58,59] first proposed the universal slope method where the slopes of the plastic and elastic lines were universalized where the fatigue strength (σ'_f) and fatigue ductility coefficient (e'_f) are dependent on tensile strength and true fracture strength [60]. Further

developments were made on the universal slope method to accurately predict the strain-life curves [61]. On the other hand, the local strain approach is commonly used to correlate the applied strain amplitude to the number of load reversals to failure using a power function [58,62–64].

The total strain amplitude can be divided into the elastic and plastic strain components, eq (2). Fatigue life can be expressed in terms of the elastic strain using the Basquin equation, eq (3), or by plastic strain using the Coffin-Manson relationship, eq (4). Therefore, the total strain amplitude vs life can be presented by eq. (5)

$$\Delta\epsilon_t/2 = \Delta\epsilon_e/2 + \Delta\epsilon_p/2 \tag{2}$$

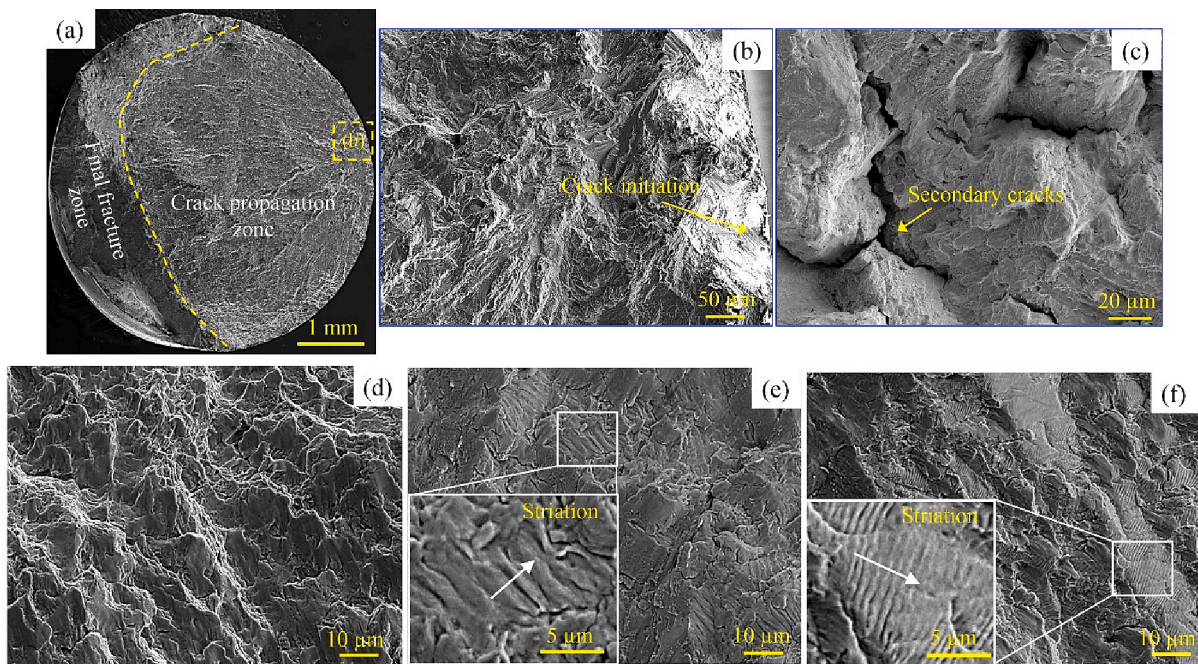


Fig. 12. SEM fractography images (a) overview of the fracture surface, (b) crack initiation from a microstructure feature, (c) secondary cracks found in the crack propagation region. Fracture surfaces of samples at different strain amplitudes ϵ_a : (d) 1.2%, (e) 0.8%, (f) 0.6%. Inset figures in (e) and (f) show the striation marks because of crack growth.

$$\Delta \varepsilon_e / 2 = \frac{\sigma_f'}{E} (2N_f)^b \quad (3)$$

$$\Delta \varepsilon_p / 2 = \varepsilon_f' (2N_f)^c \quad (4)$$

$$\Delta \varepsilon_t / 2 = \frac{\sigma_f'}{E} (2N_f)^b + \varepsilon_f' (2N_f)^c \quad (5)$$

where $\Delta \varepsilon_e / 2$ is the elastic strain amplitude, $\Delta \varepsilon_p / 2$ the plastic strain amplitude, σ_f' the fatigue strength coefficient, ε_f' the fatigue ductility coefficient, b the fatigue strength exponent, c the fatigue ductility exponent, E the elastic modulus. Fig. 11 shows the Basquin and Coffin-Manson curve fits and Table 2 shows the respective fit parameters. The parameters in Eqs. (2), (3) are derived using least-squares fitting methods of the elastic and plastic strain components respectively measured directly from the experimental data. From Fig. 11 it can be seen that there is not much difference between the elastic behaviour between the two sample orientations when the fatigue life is in the high cycle fatigue (HCF) regime. However, in the plastic strain regime, vertical samples depict a steeper curve as a result of higher ductility along this orientation. As a result, a higher fatigue ductility exponent (c) in the Coffin-Manson equation.

3.5. Fractography

The fractured samples were analysed using scanning electron microscope (SEM) to identify the fatigue crack initiation sites. Amongst all the samples tested (excluding the test runouts at fatigue life $> 10^7$ cycles), 96% samples had crack initiation from the α phase, of which 66% at the surface and 30% near the surface. Crack initiation is mainly dominated by the type of microstructure (lamellar or bi-modal), α -lamellae width and associated crystallographic texture [65]. Under cyclic loading, crack nucleation in $\alpha + \beta$ titanium alloys is attributed to the occurrence of heterogeneous deformation in the form of intense slip bands within the α phase or at α_{GB} along prior β grain. The microstructure in WAAM Ti64 consists of the Widmanstätten and colony morphology. Representative SEM fractographs are shown in Fig. 12a and 12b showing the regions of crack initiation, propagation and final failure. No defects were found in any of the sample confirming the material is fully dense. Since the resistance to dislocation motion, slip and consequently crack initiation depends on the type of microstructure and α lath width, it is difficult to identify from the fracture surfaces of this study whether the crack initiated from α or α/β interface. Nevertheless, previous studies have demonstrated that fatigue cracks nucleate along slip bands within α grains in equiaxed microstructure. In duplex structures, fatigue cracks can either initiate in the α/β lamellar interface or at the interface between the lamellar matrix and the primary α or within the primary α phase [66–70]. Based on the above, it can be deduced that the crack initiation in the current studied samples was either from α or α/β lamellar interface (Fig. 12b). All the samples showed several secondary cracks (Fig. 12c) in various directions with respect to the primary crack growth direction. In general terms, the oscillation build strategy has resulted in large and more defined single variant α colonies. The propagation of secondary cracks is the result of micro crack deflection at short length scale that is more characteristic of the size of multivariant colonies found within the coarse β grains.

Fig. 12d-f show the fracture surface features in the fatigue crack propagation regions at different strain amplitudes. The crack propagation features are similar in both sample orientations at the same strain amplitudes. Samples tested at different strain amplitude exhibits different fatigue features. Samples tested at higher strain amplitudes (i. e., 1.2%) show ductile fracture features, indicating the damage mechanism being mainly governed by the plastic deformation. On the other hand, samples tested at lower strain amplitudes (i.e. 0.8% and 0.6%) show the classic striation marks on the fracture surface indicating slow (or incremental) growth of a fatigue crack. Such striations were not

observed in samples tested at higher strain amplitude 1.2%. A general understanding (or consensus) is that each striation indicates a fatigue load cycle that propagates a fatigue crack further. The width of each striation indicates the crack growth rate [58–60]. It is apparent that the sample tested at strain amplitude 0.8% shows wider striation than sample tested at 0.6% indicating higher crack growth rate and shorter fatigue life for the former.

4. Conclusions

Cyclic deformation and fatigue behaviour of a WAAM Ti64 alloy were investigated by strain-controlled fatigue test to study the influences of sample orientation and microstructure characteristics. Tensile properties were also measured as part of the study. Based on the experimental findings and analysis, the following conclusions can be drawn:

1. Slower cooling rates associated with the oscillation build strategy have resulted in large single variant α colonies with strong crystallographic texture along the primary columnar β grain boundaries.
2. Between the two sample orientations, tensile and yield strengths are 5% higher in the direction normal to the material build direction (horizontal sample) owing to the columnar primary β grains with strong crystallographic texture along the α_{GB} that is perpendicular to the loading axis. However, elongation is reduced by 60% in the horizontal samples due to preferential failure along the α_{GB} of columnar β grain.
3. Cyclic stress softening is observed in both sample orientations when the applied strain amplitude exceeds 0.6%. Because of higher ductility, the cyclic softening rate in vertical samples is approximately two times higher when strain amplitude is higher than 0.7%. As a result, horizontal samples show slightly higher peak stress by up to 4% compared to the vertical samples.
4. In the low cycle fatigue regime ($2N_f < 10^4$ load reversals), the vertical samples' average life is about 2.5 times longer than that of the horizontal samples due to higher ductility in the former. In the high cycle fatigue regime ($2N_f > 10^4$), fatigue life property is almost isotropic.
5. SEM fractography has confirmed no porosity defects in the material as the micro-XCT result and revealed the fatigue crack initiation sources being either the α laths or α/β interface due to cyclic slip localisation. All samples have shown secondary cracks because of micro cracks deflection at short length scales in various directions with respect to the primary crack growth plane, due to the presence of large and more defined single variant α colonies. Such crack deviation has contributed to achieving higher fatigue life.

Data availability

Data underlying this study can be accessed through the Cranfield University repository at <https://doi.org/10.17862/cranfield.rd.20732050>.

CRediT authorship contribution statement

Abdul Khadar Syed: Conceptualization, Methodology, Investigation, Formal analysis, Writing – original draft. **Rob Plaskitt:** Investigation, Methodology, Formal analysis, Resources, Writing – review & editing. **Michelle Hill:** Investigation, Methodology, Formal analysis, Resources, Writing – review & editing. **Zsolt Pinter:** Methodology, Resources. **Jialuo Ding:** Methodology, Resources. **Robert Zboray:** Investigation, Methodology, Formal analysis, Resources. **Stewart Williams:** Resources, Writing – review & editing, Funding acquisition. **Xiang Zhang:** Conceptualization, Methodology, Supervision, Resources, Writing – review & editing, Funding acquisition.

Declaration of Competing Interest

The authors declare that they have no known competing financial interests or personal relationships that could have appeared to influence the work reported in this paper.

Data availability

I have shared the link to my data under the data availability statement availability

Acknowledgements

We would like to thank the UK Engineering and Physical Science Research Council (EPSRC) for supporting this research through the “New Wire Additive Manufacturing (NEWAM)” programme grant (EP/R027218/1). The Authors also thank Mark Chelu, Mark Mitchell, Alex Pierpoint, Peter Lavelle and Andrew Halfpenny from HBM Prenscia, UK, for their kind support on sample preparation, testing and valuable discussions.

References

- Leuders S, Thone M, Riemer A, Niendorf T, Troster T, Richard HA, et al. On the mechanical behaviour of titanium alloy TiAl6V4 manufactured by selective laser melting: Fatigue resistance and crack growth performance. *Int J Fatigue* 2013;48:300–7. <https://doi.org/10.1016/j.ijfatigue.2012.11.011>.
- Kasperovich G, Hausmann J. Improvement of fatigue resistance and ductility of TiAl6V4 processed by selective laser melting. *J Mater Process Technol* 2015;220:202–14. <https://doi.org/10.1016/j.jmatprotec.2015.01.025>.
- Seifi M, Salem A, Satko D, Shaffer J, Lewandowski JJ. Defect distribution and microstructure heterogeneity effects on fracture resistance and fatigue behavior of EBM Ti-6Al-4V. *Int J Fatigue* 2017;94:263–87. <https://doi.org/10.1016/j.ijfatigue.2016.06.001>.
- Hrabe N, Gnaupel-Herold T, Quinn T. Fatigue properties of a titanium alloy (Ti-6Al-4V) fabricated via electron beam melting (EBM): effects of internal defects and residual stress. *Int J Fatigue* 2017;94:202–10. <https://doi.org/10.1016/j.ijfatigue.2016.04.022>.
- Sanaei N, Fatemi A. Defects in additive manufactured metals and their effect on fatigue performance: a state-of-the-art review. *Prog Mater Sci* 2020;100:724. <https://doi.org/10.1016/j.pmatsci.2020.100724>.
- Sterling AJ, Torries B, Shamsaei N, Thompson SM, Seely DW. Fatigue behavior and failure mechanisms of direct laser deposited Ti-6Al-4V. *Mater Sci Eng A* 2016;655:100–12. <https://doi.org/10.1016/j.msea.2015.12.026>.
- Konečná R, Nicoletto G, Fintová S, Frkáň M. As-built surface layer characterization and fatigue behavior of DMLS Ti6Al4V. *Procedia Struct Integr* 2017;7:92–100. <https://doi.org/10.1016/j.prostr.2017.11.065>.
- Wycisk E, Solbach A, Siddique H, Herzog D, Walther F, Emmelmann C. Effects of defects in laser additive manufactured Ti-6Al-4V on fatigue properties. *Phys Procedia* 2014;56:371–8. <https://doi.org/10.1016/j.phpro.2014.08.120>.
- Agius D, Kourousis KI, Wallbrink C, Song T. Cyclic plasticity and microstructure of as-built SLM Ti-6Al-4V: The effect of build orientation. *Mater Sci Eng A* 2017;701:85–100. <https://doi.org/10.1016/j.msea.2017.06.069>.
- Ren YM, Lin X, Guo PF, Yang HO, Tan H, Chen J, et al. Low cycle fatigue properties of Ti-6Al-4V alloy fabricated by high-power laser directed energy deposition: Experimental and prediction. *Int J Fatigue* 2019;127:58–73. <https://doi.org/10.1016/j.ijfatigue.2019.05.035>.
- Zhang P, He AN, Liu F, Zhang K, Jiang J, Zhang DZ. Evaluation of Low Cycle Fatigue Performance of Selective Laser Melted Titanium Alloy Ti-6Al-4V. *Metals (Basel)* 2019;9. <https://doi.org/10.3390/met9101041>.
- Syed AK, Parfitt D, Wimpenny D, Muzangaza E, Chen B. Cyclic plasticity and damage mechanisms of Ti-6Al-4V processed by electron beam melting. *Int J Fatigue* 2022;160:106883. <https://doi.org/10.1016/j.ijfatigue.2022.106883>.
- Dickson JL, Boutin J, Handfield L. A comparison of two simple methods for measuring cyclic internal and effective stresses. *Mater Sci Eng* 1984;64:L7–11. [https://doi.org/10.1016/0025-5416\(84\)90083-1](https://doi.org/10.1016/0025-5416(84)90083-1).
- Syed AK, Zhang X, Davis AE, Kennedy JR, Martina F, Ding J, et al. Effect of deposition strategies on fatigue crack growth behaviour of wire + arc additive manufactured titanium alloy Ti-6Al-4V. *Mater Sci Eng A* 2021;814:141194. <https://doi.org/10.1016/j.msea.2021.141194>.
- Syed AK, Zhang X, Caballero A, Shamir M, Williams S. Influence of deposition strategies on tensile and fatigue properties in a wire + arc additive manufactured Ti-6Al-4V. *Int J Fatigue* 2021;149:106268. <https://doi.org/10.1016/j.ijfatigue.2021.106268>.
- ASTM E1382-97, standard test methods for determining average grain size using semiautomatic and automatic image analysis, in: ASTM Int., West Conshohocken, PA, 2015.
- Martina F, Colegrove PA, Williams SW, Meyer J. Microstructure of interpass rolled wire + arc additive manufacturing Ti-6Al-4V components. *Metall Mater Trans A* 2015;46:6103–18. <https://doi.org/10.1007/s11661-015-3172-1>.
- Davies PS, Wynne BP, Rainforth WM, Thomas MJ, Threadgill PL. Development of Microstructure and Crystallographic Texture during Stationary Shoulder Friction Stir Welding of Ti-6Al-4V. *Metall Mater Trans A* 2011;42:2278–89. <https://doi.org/10.1007/s11661-011-0606-2>.
- Davies PS. An investigation of microstructure and texture evolution in the Near-titanium alloy timetal 834. University of Sheffield; 2009.
- Feldkamp LA, Davis LC, Kress JW. Practical cone-beam algorithm. *J Opt Soc Am A* 1984;1:612–9. <https://doi.org/10.1364/JOSAA.1.000612>.
- ASTM E8 / E8M-16ae1, standard test methods for tension testing of metallic materials, in: ASTM Int., West Conshohocken, PA, 2016.
- ASTM E606, standard Test method for strain-controlled fatigue testing, in: ASTM Int., West Conshohocken, PA, 2021.
- Ho A, Zhao H, Fellowes JW, Martina F, Davis AE, Prangnell PB. On the origin of microstructural banding in Ti-6Al4V wire-arc based high deposition rate additive manufacturing. *Acta Mater* 2019;166:306–23. <https://doi.org/10.1016/j.actamat.2018.12.038>.
- Kelly SM, Kampe SL. Microstructural evolution in laser-deposited multilayer Ti-6Al-4V builds: Part I. Microstructural characterization. *Metall Mater Trans A* 2004;35:1861–7. <https://doi.org/10.1007/s11661-004-0094-8>.
- Baufeld B, Brandl E, Van Der Biest O. Wire based additive layer manufacturing: comparison of microstructure and mechanical properties of Ti-6Al-4V components fabricated by laser-beam deposition and shaped metal deposition. *J Mater Process Technol* 2011;211:1146–58. <https://doi.org/10.1016/j.jmatprotec.2011.01.018>.
- Al-Bermami SS, Blackmore ML, Zhang W, Todd I. The origin of microstructural diversity, texture, and mechanical properties in electron beam melted Ti-6Al-4V. *Metall Mater Trans A Phys Metall Mater Sci* 2010;41:3422–34. <https://doi.org/10.1007/s11661-010-0397-x>.
- DeRoy T, Wei HL, Zuback JS, Mukherjee T, Elmer JW, Milewski JO, et al. Additive manufacturing of metallic components – Process, structure and properties. *Prog Mater Sci* 2018;92:112–224. <https://doi.org/10.1016/j.pmatsci.2017.10.001>.
- Liu S, Shin YC. Additive manufacturing of Ti6Al4V alloy: a review. *Mater Des* 2019;164:107552. <https://doi.org/10.1016/j.matdes.2018.107552>.
- Donoghue J, Antonsamy AA, Martina F, Colegrove PA, Williams SW, Prangnell PB. The effectiveness of combining rolling deformation with wire-arc additive manufacture on β -grain refinement and texture modification in Ti-6Al-4V. *Mater Charact* 2016;114:103–14. <https://doi.org/10.1016/j.matchar.2016.02.001>.
- Antonsamy AA, Meyer J, Prangnell PB. Effect of build geometry on the β -grain structure and texture in additive manufacture of Ti6Al4V by selective electron beam melting. *Mater Charact* 2013;84:153–68. <https://doi.org/10.1016/j.matchar.2013.07.012>.
- Davis AE, Donoghue J, Kennedy JR, Byres N, Prangnell PB. In-situ observation of single variant α colony formation in Ti-6Al-4V. *Acta Mater* 2021;220:117315. <https://doi.org/10.1016/j.actamat.2021.117315>.
- Bhattacharya D, Viswanathan G, Denkenberger R, Furrer D, Fraser HL. The role of crystallographic and geometrical relationships between α and β phases in an α/β titanium alloy. *Acta Mater* 2003;51:4679–91. [https://doi.org/10.1016/S1359-6454\(03\)00179-4](https://doi.org/10.1016/S1359-6454(03)00179-4).
- Stanford N, Bate PS. Crystallographic variant selection in Ti-6Al-4V. *Acta Mater* 2004;52:5215–24. <https://doi.org/10.1016/j.actamat.2004.07.034>.
- Obasi GC, Biroseca S, Quinta Da Fonseca J, Preuss M. Effect of β grain growth on variant selection and texture memory effect during $\alpha \rightarrow \beta$ phase transformation in Ti-6 Al-4 V. *Acta Mater* 2012;60:1048–58. <https://doi.org/10.1016/j.actamat.2011.10.038>.
- Metallurgical Materials Properties Development and Standardization (MMPDS-04), 2008.
- ASTM F2924-14, Standard Specification for Additive Manufacturing Titanium-6 Aluminum-4 Vanadium with Powder Bed Fusion, in: ASTM Int., West Conshohocken, PA, 2014.
- Lütjering G, Williams J, Lütjering G, Williams J. *Titanium*. 2nd ed. Berlin Heidelberg: Springer-Verlag; 2007.
- Beese AM, Carroll BE. Review of mechanical properties of Ti-6Al-4V made by laser-based additive manufacturing using powder feedstock. *JOM* 2016;68:724–34. <https://doi.org/10.1007/s11837-015-1759-z>.
- Baufeld B, Van der Biest O, Gault R. Additive manufacturing of Ti-6Al-4V components by shaped metal deposition: Microstructure and mechanical properties. *Mater Des* 2010;31:S106–11. <https://doi.org/10.1016/j.matdes.2009.11.032>.
- Lewandowski JJ, Seifi M. Metal Additive Manufacturing: A Review of Mechanical Properties. *Annu Rev Mater Res* 2016;46:151–86. <https://doi.org/10.1146/annurev-matsci-070115-032024>.
- Zhao Z, Chen J, Lu X, Tan H, Lin X, Huang W. Formation mechanism of the α variant and its influence on the tensile properties of laser solid formed Ti-6Al-4V titanium alloy. *Mater Sci Eng A* 2017;691:16–24. <https://doi.org/10.1016/j.msea.2017.03.035>.
- Tseng JC, Huang WC, Chang W, Jeromin A, Keller TF, Shen J, et al. Deformations of Ti-6Al-4V additive-manufacturing-induced isotropic and anisotropic columnar structures: In-situ measurements and underlying mechanisms. *Addit Manuf* 2020;35:101322. <https://doi.org/10.1016/j.addma.2020.101322>.
- Carroll BE, Palmer TA, Beese AM. Anisotropic tensile behavior of Ti-6Al-4V components fabricated with directed energy deposition additive manufacturing. *Acta Mater* 2015;87:309–20. <https://doi.org/10.1016/j.actamat.2014.12.054>.
- Stapleton AM, Raghunathan SL, Bantounas I, Stone HJ, Lindley TC, Dye D. Evolution of lattice strain in Ti-6Al-4V during tensile loading at room

- temperature. *Acta Mater* 2008;56:6186–96. <https://doi.org/10.1016/j.actamat.2008.08.030>.
- [45] Pineau A, Benzerga AA, Pardoën T. Failure of metals I: Brittle and ductile fracture. *Acta Mater* 2016;107:424–83. <https://doi.org/10.1016/j.actamat.2015.12.034>.
- [46] Sun Q, Tan C, Xiao L, Sun J. Effect of size of alpha phases on cyclic deformation and fatigue crack initiation during fatigue of an alpha-beta titanium alloy. *MATEC Web Conf* 2018;165:15006. <https://doi.org/10.1051/mateconf/201816515006>.
- [47] Huang ZW, Yong PL, Zhou H, Li YS. Grain size effect on deformation mechanisms and mechanical properties of titanium. *Mater Sci Eng A* 2020;773:138721. <https://doi.org/10.1016/j.msea.2019.138721>.
- [48] Barnett MR. A rationale for the strong dependence of mechanical twinning on grain size. *Scr Mater* 2008;59:696–8. <https://doi.org/10.1016/j.scriptamat.2008.05.027>.
- [49] Salishchev GA, Galeyev RM, Valiakmetov OR, Gigliotti MFX, Bewlay BP, Hardwicke CU. Effect of deformation conditions on grain size and microstructure homogeneity of β -rich titanium alloys. *J Mater Eng Perform* 2005;14:709–16. <https://doi.org/10.1361/105994905X75493>.
- [50] Warwick JLW, Coakley J, Raghunathan SL, Talling RJ, Dye D. Effect of texture on load partitioning in Ti-6Al-4V. *Acta Mater* 2012;60:4117–27. <https://doi.org/10.1016/j.actamat.2012.03.039>.
- [51] Mathur KK, Dawson PR, Kocks UF. On modeling anisotropy in deformation processes involving textured polycrystals with distorted grain shape. *Mech Mater* 1990;10:183–202. [https://doi.org/10.1016/0167-6636\(90\)90042-E](https://doi.org/10.1016/0167-6636(90)90042-E).
- [52] Shao CW, Zhang P, Liu R, Zhang ZJ, Pang JC, Zhang ZF. Low-cycle and extremely-low-cycle fatigue behaviors of high-Mn austenitic TRIP/TWIP alloys: Property evaluation, damage mechanisms and life prediction. *Acta Mater* 2016;103:781–95. <https://doi.org/10.1016/j.actamat.2015.11.015>.
- [53] Huang Q, Hu N, Yang X, Zhang R, Feng Q. Microstructure and inclusion of Ti-6Al-4V fabricated by selective laser melting. *Front Mater Sci* 2016;10:428–31. <https://doi.org/10.1007/s11706-016-0354-8>.
- [54] Jin M, Pigionie A, Dovgyy B, Hosseini E, Hooper PA, Holdsworth SR, et al. Cyclic plasticity and fatigue damage of CrMnFeCoNi high entropy alloy fabricated by laser powder-bed fusion. *Addit Manuf* 2020;36:101584. <https://doi.org/10.1016/j.addma.2020.101584>.
- [55] Biswal R, Syed AK, Zhang X. Assessment of the effect of isolated porosity defects on the fatigue performance of additive manufactured titanium alloy. *Addit Manuf* 2018;23:433–42. <https://doi.org/10.1016/j.addma.2018.08.024>.
- [56] Carrion PE, Shamsaei N, Daniewicz SR, Moser RD. Fatigue behavior of Ti-6Al-4V ELI including mean stress effects. *Int J Fatigue* 2017;99:87–100. <https://doi.org/10.1016/j.ijfatigue.2017.02.013>.
- [57] Lunt D, da Fonseca JQ, Rugg D, Preuss M. Microscopic strain localisation in Ti-6Al-4V during uniaxial tensile loading. *Mater Sci Eng A* 2017;680:444–53. <https://doi.org/10.1016/j.msea.2016.10.099>.
- [58] Jr LF. Coffin, A Study of the Effects of Cyclic Thermal Stresses on a Ductile Metal. *Trans Am Soc Mech Eng* 1954;76:931–50.
- [59] Manson SS. Fatigue: A complex subject—Some simple approximations. *Exp Mech* 1965;5:193–226. <https://doi.org/10.1007/BF02321056>.
- [60] Ricotta M. Simple expressions to estimate the Manson-Coffin curves of ductile cast irons. *Int J Fatigue* 2015;78:38–45. <https://doi.org/10.1016/j.ijfatigue.2015.03.025>.
- [61] Muralidharan U, Manson SS. A Modified Universal Slopes Equation for Estimation of Fatigue Characteristics of Metals. *J Eng Mater Technol* 1988;110:55–8. <https://doi.org/10.1115/1.3226010>.
- [62] Basquin OH. The exponential law of endurance tests. *Am Soc Test Mater Proc* 1910;10:625–30.
- [63] S.S. Manson, Behavior of Materials Under Conditions of Thermal Stress, Technical Report TN 2933, Boston, USA, 1953.
- [64] Suresh S. Fatigue of Materials. Cambridge 1998. <https://doi.org/10.1017/CBO9780511806575>.
- [65] Hall JA. Fatigue crack initiation in alpha-beta titanium alloys. *Int J Fatigue* 1997;19:23–37. [https://doi.org/10.1016/S0142-1123\(97\)00047-9](https://doi.org/10.1016/S0142-1123(97)00047-9).
- [66] Leyens MPC. Titanium and Titanium Alloys: Fundamentals and Applications. Wiley-VCH Verlag GmbH & Co. KGaA; 2005.
- [67] Benson DK, Grosskreutz JC, Shaw GG. Mechanisms of fatigue in mill-annealed Ti-6Al-4V at room temperature and 600°F. *Metall Trans* 1972;3:1239–48. <https://doi.org/10.1007/BF02642458>.
- [68] Kerr WR, Eylon D, Hall JA. On the correlation of specific fracture surface and metallographic features by precision sectioning in titanium alloys. *Metall Trans A* 1976;7:1477–80. <https://doi.org/10.1007/BF02658839>.
- [69] Zhai Y, Galarraga H, Lados DA. Microstructure, static properties, and fatigue crack growth mechanisms in Ti-6Al-4V fabricated by additive manufacturing: LENS and EBM. *Eng Fail Anal* 2016;69:3–14. <https://doi.org/10.1016/j.engfailanal.2016.05.036>.
- [70] Bantounas I, Dye D, Lindley TC. The role of microtexture on the faceted fracture morphology in Ti-6Al-4V subjected to high-cycle fatigue. *Acta Mater* 2010;58:3908–18. <https://doi.org/10.1016/j.actamat.2010.03.036>.